communications physics

ARTICLE

https://doi.org/10.1038/s42005-023-01464-x OPEN

Possible strain-induced enhancement of the superconducting onset transition temperature in infinite-layer nickelates

Xiaolin Ren[1,2], Jiarui Li[3], Wei-Chih Chen[4], Qiang Gao[1], Joshua J. Sanchez[3], Jordyn Hales[5], Hailan Luo[1,2], Fanny Rodolakis[6], Jessica L. McChesney[6], Tao Xiang[1,7], Jiangping Hu[1,8], Riccardo Comin[3], Yao Wang[4,5✉], Xingjiang Zhou[1,2,7,8✉] & Zhihai Zhu[1,2,8✉]

The mechanism of unconventional superconductivity in correlated materials remains a great challenge in condensed matter physics. The recent discovery of superconductivity in infinite-layer nickelates, as an analog to high-T_c cuprates, has opened a new route to tackle this challenge. By growing 8 nm $Pr_{0.8}Sr_{0.2}NiO_2$ films on the $(LaAlO_3)_{0.3}(Sr_2AlTaO_6)_{0.7}$ substrate, we successfully raise the superconducting onset transition temperature T_c in the widely studied $SrTiO_3$-substrated nickelates from 9 K into 15 K, which indicates compressive strain is an efficient protocol to further enhance superconductivity in infinite-layer nickelates. Additionally, the x-ray absorption spectroscopy, combined with the first-principles and many-body simulations, suggest a crucial role of the hybridization between Ni and O orbitals in the unconventional pairing. These results also suggest the increase of T_c be driven by the change of charge-transfer nature that would narrow the origin of general unconventional superconductivity in correlated materials to the covalence of transition metals and ligands.

[1] Institute of Physics, National Laboratory for Condensed Matter Physics, Chinese Academy of Sciences, 100190 Beijing, China. [2] School of Physical Sciences, University of Chinese Academy of Sciences, 100049 Beijing, China. [3] Department of Physics, Massachusetts Institute of Technology, Cambridge, MA 02139, USA. [4] Department of Physics and Astronomy, Clemson University, Clemson, SC 29631, USA. [5] Department of Chemistry, Emory University, Atlanta, GA 30322, USA. [6] X-Ray Science Division, Advanced Photon Source, Argonne National Laboratory, Lemont, IL 60439, USA. [7] Beijing Academy of Quantum Information Sciences, 100193 Beijing, China. [8] Songshan Lake Materials Laboratory, Dongguan 523808, China. ✉email: yao.wang@emory.edu; XJZhou@iphy.ac.cn; zzh@iphy.ac.cn

The discovery of the high-T_c superconducting cuprates is one of the greatest surprises in quantum materials. Due to the complexity stemming from multiple intertwined orders, the pairing mechanism of cuprates remains an enigma[1]. Many theories have proposed that the unconventional superconductivity is likely associated with the strong correlation nature of the *d*-orbital electrons in transition-metal oxides (TMOs)[2], which can be characterized by the Mott insulating parent state at the filling of one hole per unit cell. This picture has motivated the study of superconductivity in several TMOs and, more recently, magic-angle twisted bilayer graphene[3]. However, the anticipated analogy materials, such as iridates and ruthenates, do not show high T_c as cuprates. Theoretically, it remains a question whether the single-band Hubbard model, as a prototype of correlated electron systems, indeed gives long-range ordered superconductivity[4,5].

The recent discovery of superconducting nickelates provides a new opportunity to shed light on the puzzle[6–11]. Due to nickelates' structural and chemical similarities with cuprates, a comparative study of these two materials may help establish the pairing mechanism and guide us to design materials with higher T_c[12–23]. Experiments have shown infinite-layer nickelates exhibiting similar magnetic excitations with cuprates[24]. However, nickelates show a much lower T_c. A possible reason is that the nickelates $RNiO_2$ (R = La, Pr, and Nd) are Mott-Hubbard insulators[18,22,25,26], while cuprates are charge-transfer insulators with more covalent-bond nature near the parent compound. The charge-transfer property of the latter is characterized by a prominent pre-peak in the oxygen *K*-edge x-ray absorption spectrum (XAS), usually referred to as the Zhang-Rice peak[27]. Given that the charge-transfer gap was also found to anti-correlate (and thus are indirectly proportional) with T_c in various cuprate compounds[28,29], it is conceivable that the oxygen-orbital components of dopants may play a crucial role in pairing. A critical step to assess this is to manipulate the charge-transfer extent of nickelates and demonstrate the possibility of enhancing superconductivity[30–32].

Here, we report an enhancement of T_c by growing the $Pr_{0.8}Sr_{0.2}NiO_2$ film on a compressive substrate $(LaAlO_3)_{0.3}(Sr_2AlTaO_6)_{0.7}$ (LSAT). Combining first-principles and many-body simulations, we reveal that the in-plane compressive strain strengthens the $p-d$ hybridization between oxygen and nickel orbitals. Thus, a considerable number of doped carriers distribute into oxygen orbitals, increasing the pre-peak in the oxygen *K*-edge XAS. This comparison reflects the dominant role of the charge-transfer nature in unconventional superconductivity, including but not restricted to nickelates and cuprates. This comparative study of the impact of microscopic ingredients on T_c further motivates a systematic and efficient approach to designing superconductivity in TMOs.

Results and discussion

Substrate-induced strain and enhanced T_c. As illustrated in Fig. 1a, b, we prepared $Pr_{0.8}Sr_{0.2}NiO_2$ films of equal thickness (8 nm) on two different substrates, $SrTiO_3$ and LSAT, using pulsed laser deposition (PLD) followed by a CaH_2-assisted chemical reduction method (see Supplementary Note 1 for details). Figure 1c, d shows the high-angle annular dark-field (HAADF) scanning transmission electron microscopy (STEM) images of the two superconducting $Pr_{0.8}Sr_{0.2}NiO_2$ films on the two substrates, respectively. The contrast difference of diffraction spots reveals the uniform growth of the films with an ordered structure of a coherent infinite layer, displaying no evidence of minority phases. The well-defined infinite-layer phase of the $Pr_{0.8}Sr_{0.2}NiO_2$ films is further disclosed in the annular bright-field (ABF) STEM images in Fig. 1e, f. The enlarged views of the areas inside the rectangles in Fig. 1e, f are shown in Fig.1g, h for better visibility of the lattice structures of the films and the substrates near the interface. The clear and sharp interfaces between the films and the substrates confirm the former epitaxially strained on the latter. Besides, the reciprocal space maps (RSM) around the (103) reflection demonstrate that the films are strained to the substrates (see Supplementary Note 2 for details). Based on both measurements, the in-plane lattice constants of the nickelate films match those of the substrates, i.e., a = 3.868 Å, yielding −1% compressive in-plane strain in the films grown on LSAT compared to $SrTiO_3$[10].

With the nickelate films on distinct substrates, we first examine their transport properties using a Quantum Design Physical Property Measurement System (PPMS) with a standard four-probe configuration. Figure 2a shows the temperature-dependent resistivity of these two $Pr_{0.8}Sr_{0.2}NiO_2$ films on $SrTiO_3$ and LSAT substrates, respectively. Both films exhibit a sudden decrease in resistivity, characteristic of the superconducting transition (see Supplementary Note 3 for similar measurements on more samples). Here, we employ the onset temperature to quantify the superconductivity critical temperature T_c, resulting in $T_c^{(onset)} = 9$ K and 15 K (highlighted with arrows) for samples grown on $SrTiO_3$ and LSAT, respectively. To further confirm the superconducting behavior, we investigate the transport properties with a magnetic field (up to 9.0-tesla) applied perpendicular to the ab-plane of the film. As shown in Fig. 2c, d, the field dependence exhibits similar behaviors: In the normal state, the films display negligible variation, whereas, below the superconducting transition, the conductance is suppressed significantly with an increasing magnetic field.

We summarize the critical temperatures of various nickelate experiments by the gray area in Fig. 2b to compare with previous experiments. Considering the sensitivity to the thickness, we further mark the T_c varying from 7 K to 12 K for existing $Pr_{0.8}Sr_{0.2}NiO_2$ studies[9]. The $T_c^{(onset)} \approx 9$ K (denoted by the red diamond) of our 8 nm-thick uncapped $Pr_{0.8}Sr_{0.2}NiO_2$ film grown on $SrTiO_3$ is lower than $T_c^{(onset)} \approx 12$ K from the previous studies on the film with equal thickness. Interestingly, when substrated by LSAT, the same uncapped 8 nm-thick $Pr_{0.8}Sr_{0.2}NiO_2$ film exhibits a considerably higher $T_c^{(onset)} \approx 15$ K, beyond the record of any (capped and uncapped) STO-substrated samples for the same doping. The uncapped films on both substrates in our study show a more significant broadening of superconducting transition, which is probably due to the detailed topotactic reduction and common in various superconducting nickelate films[11,33]. Nevertheless, the zero resistance develops at 2.0 K and 2.5 K in zero-field for the films on $SrTiO_3$ and LSAT, respectively. It is noticed that such an observation of enhanced T_c was also reported in $Nd_{1-x}Sr_xNiO_2$ films on LSAT compared to those on $SrTiO_3$ for different doping levels[34]. While we cannot completely rule out some other extrinsic effects such as crystalline disorder that might partially affect T_c, it seems natural to attribute this $T_c^{(onset)}$ enhancement in the comparative study to the crystal structure of $Pr_{0.8}Sr_{0.2}NiO_2$, which is compressively strained by the LSAT substrate. We were aware that an even higher $T_c^{(onset)} \approx 17$ K was reported in $Pr_{0.82}Sr_{0.18}NiO_2$/STO[35], which does not necessarily conflict with our attribution of the enhancement to strain since it corresponds to a different doping level that expects to result in a higher $T_c^{(onset)}$ than that of $Pr_{0.80}Sr_{0.20}NiO_2$/STO[10]. Besides, the capping of STO layers may help improve the sample quality.

Pre-edge peak in x-ray absorption spectra. To unveil the connection between the strain and the enhancement of T_c in $Pr_{0.8}Sr_{0.2}NiO_2$/LSAT, we further examine their electronic

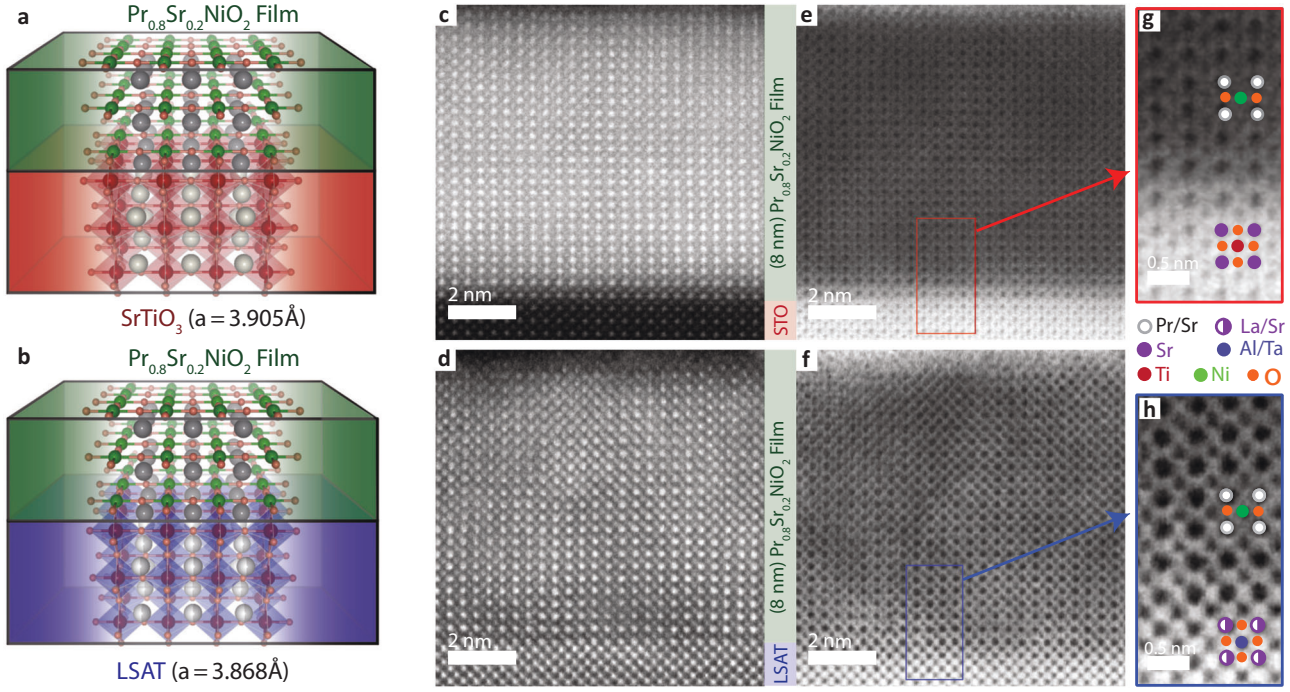

Fig. 1 Cross-sectional scanning transmission electron microscopy (STEM) images of two types of superconducting $Pr_{0.8}Sr_{0.2}NiO_2$ films. a, **b** The schematic illustrations of heterostructures of $Pr_{0.8}Sr_{0.2}NiO_2$ films on two different substrates $SrTiO_3$ and $(LaAlO_3)_{0.3}(Sr_2AlTaO_6)_{0.7}$ (LSAT) respectively. **c**, **d** The high-angle annular dark field (HAADF) STEM images of films on $SrTiO_3$ and LSAT substrates, respectively. **e**, **f** The annular bright field (ABF) STEM images of film on $SrTiO_3$ and LSAT substrates, respectively. **g**, **h** The enlarged views of the areas inside the rectangles in (**e**, **f**), respectively.

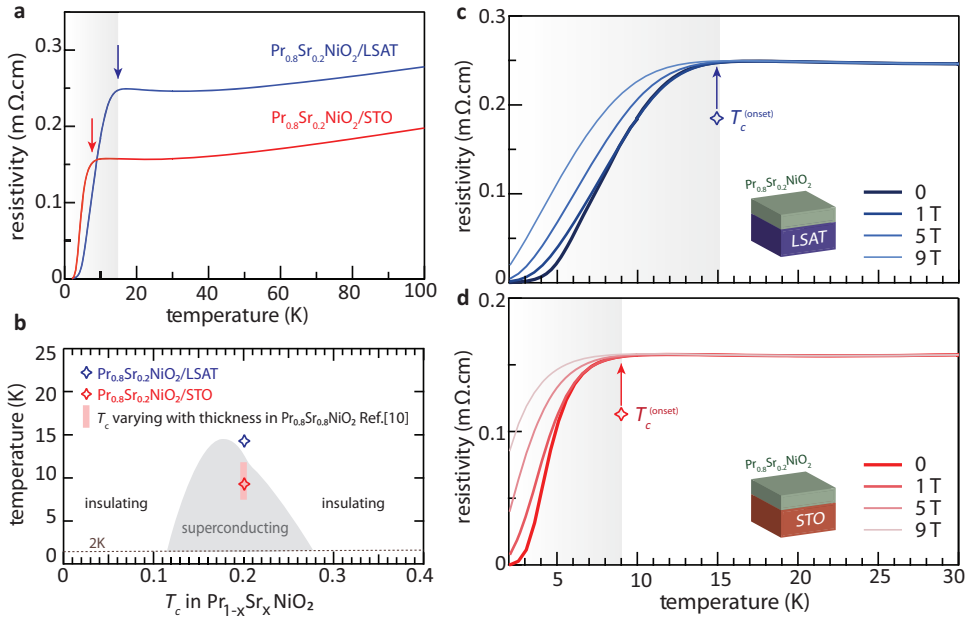

Fig. 2 Transport properties of superconducting $Pr_{0.8}Sr_{0.2}NiO_2$ films on two different substrates. a Temperature-dependent resistivity of the $Pr_{0.8}Sr_{0.2}NiO_2$ on $SrTiO_3$ and $(LaAlO_3)_{0.3}(Sr_2AlTaO_6)_{0.7}$ (LSAT) substrates, respectively. **b** The phase diagram of $Pr_{1-x}Sr_xNiO_2$ films adapted from Ref. [10] The T_c varies from 7 K to 12 K with thickness for $Pr_{0.8}Sr_{0.2}NiO_2$ films adapted from Ref. [9] (pink bar). The $T_c^{(onset)} \approx 9$ K (red diamond) and $T_c^{(onset)} \approx 15$ K (blue diamond) of our 8 nm-thick uncapped $Pr_{0.8}Sr_{0.2}NiO_2/SrTiO_3$ and $Pr_{0.8}Sr_{0.2}NiO_2$/LSAT. **c**, **d** Magnetic-field response of superconducting $Pr_{0.8}Sr_{0.2}NiO_2$ film on $SrTiO_3$ and LSAT substrates, at a varying magnetic field perpendicular to the (**a**, **b**) plane. The onset of superconducting transition at 9 K for the film on $SrTiO_3$ is smaller than that of the film at 15 K on LSAT substrate. Zero-resistance is obtained at 2.5 K and 2.0 K for the films on LSAT and $SrTiO_3$, respectively.

structure using XAS. The XAS at the Ni $L_{3,2}$ and Pr $M_{5,4}$ absorption edges have been collected for $Pr_{0.8}Sr_{0.2}NiO_2$ films to characterize the ionic valence states (see Supplementary Note 4 for further details). We select the O *K*-edge to reveal the nature of dopant carriers since its characteristic peaks have been regarded as a fingerprint in cuprates[27]. Considering that the top layer of the films can be oxidized due to air exposure as well as that the substrates are insulators, we have employed the total fluorescence

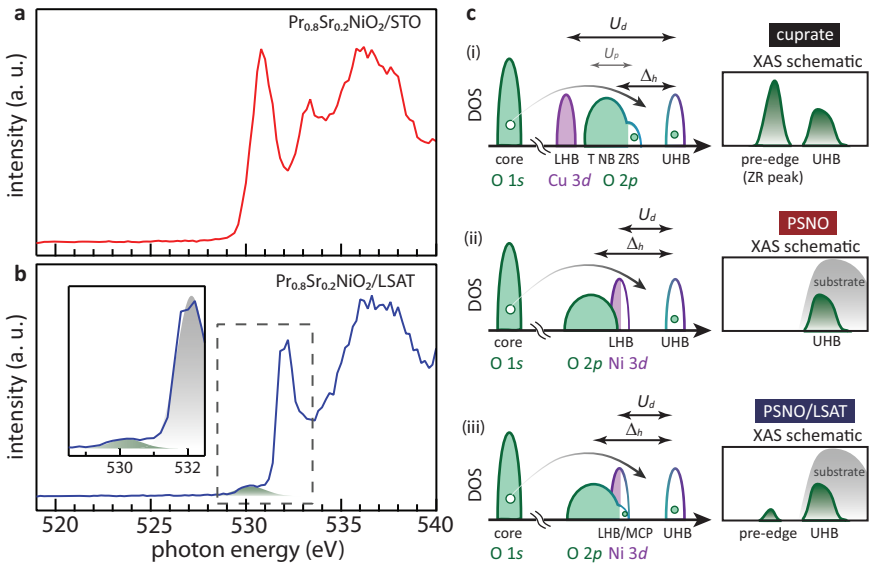

Fig. 3 Total fluorescence-yield x-ray absorption spectra (XAS) of two superconducting nickelate films. a, **b** The XAS at the O *K* edge of $Pr_{0.8}Sr_{0.2}NiO_2$ thin films with the linear polarization perpendicular to the films' *c* axis. The inset in (**b**) shows the fitted spectral features near the pre-edge peak (the regime inside of the dashed square). The mobile carrier peak (MCP) is absent in the film on $SrTiO_3$ substrate of (**a**). **c** Schematic density of states (DOS) of transition-metal oxides (TMOs) and their corresponding XAS features (i): a charge-transfer insulator, represented by cuprates, distributes doped holes primarily to oxygen orbitals, resulting in a prominent pre-edge peak in XAS; (ii): a Mott-Hubbard insulator, represented by nickelates on STO substrates, distributes doped holes primarily to transition-metal 3*d* orbitals, resulting in negligible pre-edge peaks; (iii): strained nickelates exhibit stronger hybridization between 3*d* and 2*p* orbitals, producing a pre-edge peak. UHB and LHB represent the upper and lower Hubbard bands, respectively.

yield (TFY) mode to collect the XAS at the oxygen *K* absorption edge. Similar to other recent studies, we find that the *K*-edge XAS of $Pr_{0.8}Sr_{0.2}NiO_2/SrTiO_3$ does not exhibit any pre-edge peak[22,36], suggesting that the parent compound of superconducting nickelates ($Pr_{0.8}Sr_{0.2}NiO_2/SrTiO_3$) falls into the Mott-Hubbard insulator regime. This property is in sharp contrast to cuprates, where an extra pre-edge mobile carrier peak (MCP) arises with hole doping and carries intensity comparable with the doping concentration. We illustrate the difference in XAS features via the partial density of states (PDOS) distribution sketched in Fig. 3c. As charge-transfer insulators, cuprates have a relatively strong on-site Coulomb interaction U_d (primarily for the Cu 3*d* electrons) compared to the charge-transfer energy Δ_h in the hole language. Therefore, a doped hole primarily occupies the oxygen 2*p* orbital, which hybridizes with the Cu 3*d* orbital as the Zhang-Rice singlet band. XAS selectively probes the unoccupied PDOS on oxygen, resulting in the coexistence of the pre-edge MCP and the upper Hubbard band (UHB) peaks. Nevertheless, the Δ_h is slightly larger than the U_d in nickelates, leading to tiny dopant holes on oxygen orbitals and, accordingly, a main absorption peak with a shoulder instead of a pre-edge peak. It is important to note that the distinction between charge-transfer and Mott-Hubbard insulators occurs suddenly at $\Delta_h \sim U_d$ only in the atomic limit[25], while the presence of orbital hybridization leads to a crossover in the intensity of the pre-edge peak (see Supplementary Note 5 for detailed discussions).

Unlike the STO-substrated nickelates, the XAS of our $Pr_{0.8}Sr_{0.2}NiO_2$/LSAT sample exhibits an evident pre-peak to the O *K* main edge at 530.2 eV, reminiscent of the pre-peaks in cuprates[27]. The energy position of 530.2 eV for the pre-peak is nearly equal to the observed hybridization peak in $La_4Ni_3O_8$, which belongs to another family of nickelate materials ($R_{n+1}Ni_nO_{2n+2}$)[37]. Therefore, we can attribute this pre-edge peak in $Pr_{0.8}Sr_{0.2}NiO_2$/LSAT to the MCP. Since the charge-transfer nature appears to be one of the most significant differences between cuprates and nickelates, the emergence of the pre-edge XAS peak in LSAT-substrated nickelates provides insight for its enhanced T_c, consistent with previous results[28,29,38].

Numerical explanation of the electronic structure's change. To reveal the impact of the strained lattice on nickelates' electronic structure, we simulate the doped carriers and spectral evolution upon straining using density functional theory (DFT) and the extracted many-body model. We first calculate the electronic structure of the pristine and −1% strained $PrNiO_2$ using Perdew-Burke-Ernzerhof (PBE) functional (see Methods). As shown in Fig. 4, the simulated PDOS reflects that the highest occupied molecular orbital (HOMO) and the lowest unoccupied molecular (LUMO) orbitals primarily consist of Ni $3d_{x2-y2}$ orbitals. As pointed out in previous studies[22], the rare-earth band also resides at low energy, leading to a "self-doping" effect. To address the experimental features observed in the oxygen *K*-edge XAS, we focus on the oxygen components of the electronic wavefunction. By projecting the simulated Kohn-Sham orbitals to single-particle Wannier orbitals, we extracted two oxygen orbitals ($2p_x$ and $2p_y$) which hybridize with the active Ni $3d_{x2-y2}$ orbital [see the inset of Fig. 4a]. We employ these three orbitals to construct a tight-binding model, the first four terms in Eq. (1) in the Methods section, where the hopping parameters and site energies are extracted from the Kohn-Sham Wannier orbitals. For the pristine $PrNiO_2$, we obtain $t_{pd} = 1.36$ eV, $t_{pp} = 0.57$ eV, and $E_d - E_p = 3.90$ eV, consistent with previous simulations[22] for the −1% strained $PrNiO_2$, t_{pd} are increased into 1.41 eV, while the changes of other parameters are less than 2%.

We then involve the strong Coulomb interactions, doping, and x-ray core-hole interactions on top of the DFT-extracted model to simulate the XAS spectra and analyze correlation effects. Based on the estimations from previous studies, we set the Hubbard-type Coulomb interactions on the Ni 3*d* and O 2*p* orbitals as $U_d = 6$ eV and $U_p = 2$ eV, respectively. We also set the core-hole attractive interaction $U_c = 3$ eV to match the experimental separation between the pre-edge and main absorption peaks. The XAS spectral intensity is simulated using Eq. (2) in the Methods section. As shown in Fig. 4b, we manipulate the strength of t_{pd} and fix other parameters, mimicking the primary impact on the electronic structure induced by the strain effect. Considering

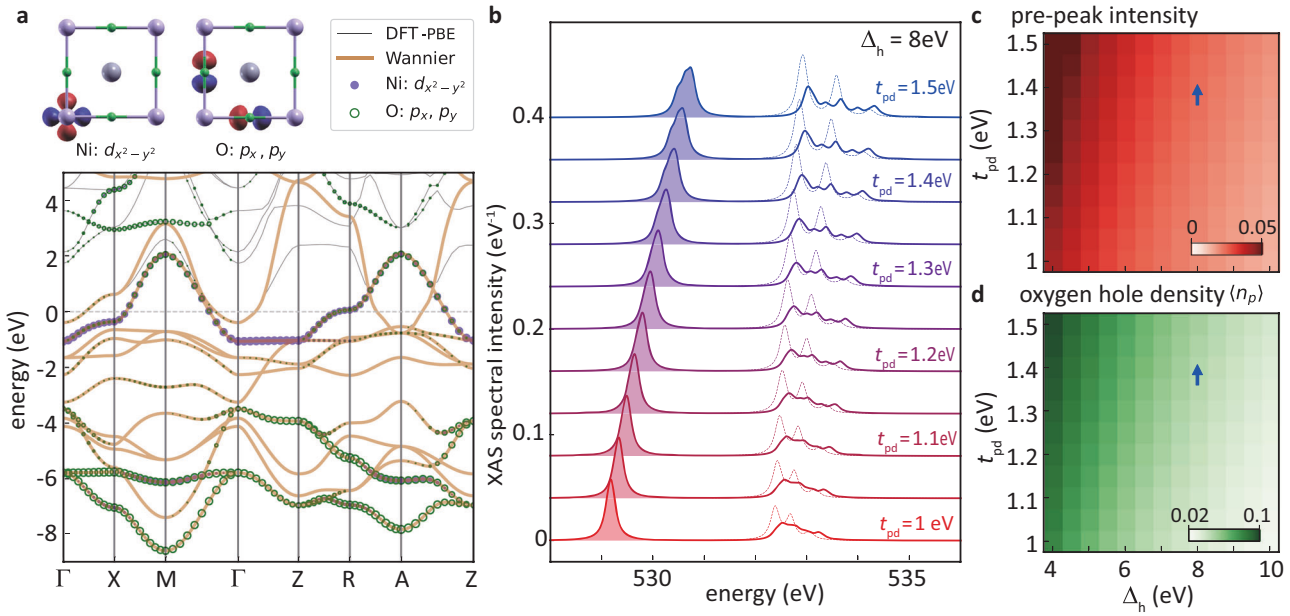

Fig. 4 Theoretical analysis of strain effects on the electronic structures and x-ray absorption spectra (XAS) of Praseodymium Nickelates. a Band structures of unstrained $PrNiO_2$ from density functional theory (DFT) and Wannier tight-binding model. Nickel's $3d_{x2-y2}$ and oxygen's p_x and p_y orbitals are shown at the top, where gray, purple, and green spheres represent Pr, Ni, and O, respectively. The site energies of E_d and E_p, as well as the hopping parameters t_{pd} (hopping between Ni: $3d_{x2-y2}$ and O: p_x, p_y) and t_{pp} (hopping between O: p_x and p_y) in the Wannier tight-binding model. These band parameters are employed in exact diagonalization simulations. **b** Exact diagonalization XAS with a charge-transfer energy $\Delta_h = 8$ eV and a varying t_{pd} from 1.0 eV to 1.5 eV. The dashed and solid lines represent the spectra for 0 and 12.5 % hole-doping, respectively. The pre-peak area (illustrated by the shade) increases with an increasing t_{pd}. The pre-peak area (**c**) and the average hole number per $p_{x,y}$ orbital (**d**) as a function of Δ_h and t_{pd} are shown by the intensity plots. Both increase with an increasing t_{pd} and a decreasing Δ_h. The blue arrows indicate the change of t_{pd} from 1.36 to 1.41 eV when 1 % compressive epitaxial strain is applied.

possible ambiguities of band parameters extracted from minimal Wannier-folded orbitals, we examine the spectral properties for a wide range of t_{pd} values, from 1.0 to 1.5 eV. The simulated XAS results suggest that increased t_{pd}, induced by the compressive strain effect, enhances the pre-edge peak, consistent with our experimental observations in Fig. 3a, b. As illustrated in Fig. 3c, although the strain does not switch the relative size of U_d to Δ_h in the atomic representation, the increased t_{pd} mixes oxygen and nickel PDOS at the top of the lower Hubbard band (LHB). Therefore, a larger portion of the doped holes resides in oxygen, resulting in the rise of the pre-edge XAS peak.

To further demonstrate the aforementioned mechanism, we calculate the average hole concentrations ⟨n_p⟩ on the oxygen $2p_{x/y}$ orbitals. By comparing the undoped and doped XAS results, the pre-edge peak reflects most dopant carrier concentrations in oxygen. Therefore, we evaluate the pre-peak intensity and ⟨n_p⟩ for a wide range of charge-transfer energy Δ_h and t_{pd} of the three-band Hubbard model. As shown in Fig. 4c, d, the parameter dependencies of these two quantities are consistent in the entire $\Delta_h - t_{pd}$ parameter space. We also highlight the DFT-extracted model parameters for the pristine and strained nickelates to guide the eye. In this context, the pre-edge peak intensity (Fig. 4c) rises by 2.8%, and the oxygen-hole concentration (Fig. 4d) increases by 3.1%. This increase is smooth in the DFT-extracted model, in contrast to the sharp transition in the atomic model (see Supplementary Note 5), but the correlation between the spectral and carrier properties is the same. Due to the simplicity of the downfolded three-band, our simulation has neglected contributions from other oxygen orbitals in nickelates and substrates, underestimating the main-peak intensity. Despite the mismatch of this main peak, the rise of the pre-edge peak reflects that the nickelates in LSAT substrate distribute more dopant carriers into oxygen orbitals.

The fact that $Pr_{0.8}Sr_{0.2}NiO_2$/LSAT displays a much higher T_c compared with $Pr_{0.8}Sr_{0.2}NiO_2$/STO suggests the strain enabled via substrate design is an efficient route to control, and especially enhance, the superconductivity in nickelates. More importantly, the comparison between strained and unstrained nickelates, as well as nickelates and cuprates, provides significant insights into the long-standing puzzle – the pairing mechanism of unconventional superconductivity in correlated materials. Our experimental evidence for the concurrent rise of T_c and the emergence of the pre-edge peak in oxygen K-edge XAS reflects the intrinsic connection between the TM-oxygen hybridization in the pairing mechanism. Narrowing the dominant factor into the hybridization, one can further interpret its microscopic origin. A possible explanation is the enhanced spin fluctuations due to these Ni-O hybridizations, similar to the recently observed strained-enhanced magnons in monolayer cuprates[39]. According to our first-principles extracted three-band models, we simulate the dynamical spin structure factors of the pristine and strained $PrNiO_2$. The top of magnon excitations rises from 178 meV into 192 meV with the −1% compressive strain (see Supplementary Note 6 for further details). Large-momentum spin fluctuations have been popular candidates for the d-wave pairing glue of unconventional superconductivity. Moreover, such a 7.8% increase of spin excitations out of the 1% strain indicates the outsized nonlinear impact of the lattice structure. Thus, an alternative but non-exclusive explanation for the 60% enhancements lies in the possible contribution of electron-phonon to unconventional superconductivity[40–45]. As a key difference from nickelates and other TMOs[26], the unique charge-transfer insulating parent compounds of cuprates cause doped holes primarily to reside on oxygen, whose vibrations constitute most phonon modes. The present experimental and simulation results suggest that the strain-enhanced hybridization between O and Ni

orbitals also leads to the similar charge transfer of doped carriers, which may further help pairing.

It is still challenging to examine if the magnetic or phonon-assisted mechanism, or their combined effect, may account for the more than 60% enhancement of T_c in $Pr_{0.8}Sr_{0.2}NiO_2$/LSAT. The quantitative assessment of their contributions may identify the general pairing mechanism in correlated materials and motivates future experiments. For example, resonant inelastic x-ray scattering has characterized both the magnon and phonon dispersions in STO-substrated $Nd_{1-x}Sr_xNiO_2$[24]. Comparative RIXS studies of nickelates on these two substrates may provide more insight into individual contributions from these excitations. Thus, our results, together with the further investigations of pairing mechanisms, should stimulate systematic engineering and design of high-T_c superconductivity.

Methods

Sample preparation and experimental characterization. The perovskite precursor $Pr_{0.8}Sr_{0.2}NiO_3$ films were prepared by using pulsed laser deposition (PLD). The corresponding infinite-layer phase was acquired by the soft-chemistry reduction method. The superconducting transition temperature was confirmed by transport measurements using a Quantum Design Physical Property Measurement System (PPMS) with a standard four-probe configuration. Samples for the cross-sectional scanning transmission electron microscopy (STEM) were prepared by focused ion beam (FIB, Helios 600i) techniques. The high-angle annular dark field (HAADF) and annular bright field (ABF) STEM images were acquired on the ARM-200F (JEOL, Japan) operated at 200 kV with a CEOS Cs corrector (CEOS GmbH, Germany). The x-ray absorption spectroscopy (XAS) measurements were performed at beamline 29-ID IEX at the Advanced Photon Source, Argonne National Laboratory. The beamline uses an electromagnetic undulator providing a soft x-ray from 250 eV to 3000 eV. The spectra were normalized by the incident x-ray intensity (I0) using a drain current from a gold mesh upstream of the sample. All spectra were collected at 30 K.

Density functional theory calculations. The electronic band structure of $PrNiO_2$ is calculated using the Quantum Espresso package[46] with Perdew-Burke-Ernzerhof[47] exchange-correlation functional, where the pseudopotential is based on the projected augmented wave (PAW) method[48]. We adopt the Monkhorst-Pack sampling[49] with a Γ-centered k-mesh of $13 \times 13 \times 15$ and a plane-wave cutoff energy of 40 rydberg is used to expand the wave function. The convergence criteria of structure relaxation and self-consistent field are set to 10^{-4} rydberg/bohr and 10^{-7} rydberg, respectively. For the −1% strained structure, we then change the lengths of the a- and b-axis directly while the *c*-axis remains unchanged.

To extract the site energies and hopping parameters, we employ the Wannier90 package[50] to fit our DFT results and construct the tight-binding models, where a total number of 16 Wannier functions: five Pr's *d* orbitals, five Ni's *d* orbitals, and six O's *p* orbitals, are considered. In our calculations, the disentanglement procedure is employed with an energy window from −10 to +0.8 eV.

Exact diagonalization simulation for XAS spectra. We employ the three-band Hubbard model extracted from the DFT Wannier orbitals as a minimal description of the charge-transfer physics in PSNO. The Hamiltonian reads as:

$$\begin{aligned} Hv = &- \sum_{\langle i,j\rangle\alpha\sigma} t_{pd}^{ij}(d_{i\sigma}^{+}p_{j\alpha\sigma} + h.c.) \\ &- \sum_{\langle j,j'\rangle\sigma} t_{pp}^{jj'}(p_{jx\sigma}^{+}p_{j'y\sigma} + h.c.) + \sum_{i\sigma} E_d n_{i\sigma}^{d} + \sum_{j\alpha\sigma} E_p n_{j\alpha\sigma}^{p} \\ &+ \sum_{i} U_d n_{i\uparrow}^{d} n_{i\downarrow}^{d} + \sum_{j\alpha} U_p n_{j\alpha\uparrow}^{p} n_{j\alpha\downarrow}^{p}, \end{aligned} \quad (1)$$

Here, $d_{i\sigma}^{+}(p_{j\alpha\sigma}^{+})$ creates an electron with spin σ at a Ni site i (O site j), and $n_{i\sigma}^{d}(n_{j\sigma}^{p})$ is the Ni (O) electron number. The flavor $\alpha = \{x, y\}$ labels the $2p_{x,y}$ orbitals. The t_{pd} and t_{pp} determine the nearest-neighbor hopping amplitudes, and E_d (E_p) is the electronic site energy. These single-particle parameters are extracted from the Wannier orbitals of the DFT simulation. The last two terms are the on-site Hubbard interactions, whose strengths are set as ad hoc parameters $U_d = 6$ eV, $U_p = 2$ eV, comparable with previous studies[22,26]. The charge-transfer energy in the hole representation is defined as $\Delta_h = E_d - E_p + U_d - U_p$. At the pristine PSNO, the DFT simulation gives $\Delta_h = 8$ eV, $|t_{pd}| = 1.36$ eV, $|t_{pp}| = 0.57$ eV, while in the −1% strained PSNO, the extracted parameters of $|t_{pd}|$ and $|t_{pp}|$ are = 1.41 eV and 0.58 eV. Beyond the single-particle Kohn-Sham band parameters, we perform many-body simulations for the XAS spectrum of the three-orbital Hubbard model on an 8-site cluster for two different doping levels: 0% (half-filling) and 12.5% (underdoped).

The many-body ground state $|G\rangle$ of the three-band valence-electron Hamiltonian Eq. (1) is solved by the exact diagonalization (ED). With this ground state, the zero-temperature XAS spectrum is calculated using

$$I_{XAS}(\omega, T) = -\frac{1}{\pi}\mathrm{Im}\langle G|D^{+}\frac{1}{\omega + E_G - H + i\delta}D|G\rangle, \quad (2)$$

where E_G is the ground-state energy and δ is the broadening corresponding to the inverse lifetime of the intermediate state. For the convenience of extracting the integrated peak intensity, we employed a small broadening $\delta = 0.1$ eV in the simulation, where realistic values should be much larger. Different from the three-band valence-electron Hamiltonian in Eq. (1), the intermediate-state Hamiltonian H in Eq. (2) describes an x-ray excited state and is defined in an extended Hilbert space consisting of both the valence electrons and a single core-level band resonant to the x-ray edge. Thus, the dipole operators D define the electron transition between the oxygen 1 *s* (core-level) and the 2*p* orbitals (valence level) selected by the x-ray *K*-edge edge

$$D = \sum_{\alpha\sigma} p_{j\alpha\sigma}^{+} c_{j\sigma}, \quad (3)$$

We ignore the matrix elements since we do not compare absolute intensities among different edges. In addition to the valence-band tight-binding model H_v, the intermediate state in Eq. (2) contains an extra core hole and its attractive interaction

$$H_c = \sum_{i\sigma} E_{edge}(1 - n_{i\sigma}^{c}) - U_c \sum_{i\sigma\sigma'} n_{i\sigma}^{p}(1 - n_{i\sigma'}^{c}), \quad (4)$$

where E_{edge} is the edge energy $E_{edge} = 530$ eV and $U_c = 3$ eV the core-hole potential.

Data availability

The data that support the plots within this paper and other findings of this study are available from https://doi.org/10.6084/m9.figshare.24522937.v1.

Received: 9 August 2023; Accepted: 13 November 2023;
Published online: 27 November 2023

References

1. Keimer, B., Kivelson, S. A., Norman, M. R., Uchida, S. & Zaanen, J. From quantum matter to high-temperature superconductivity in copper oxides. *Nature* **518**, 179–186 (2015).
2. Dagotto, E. Correlated electrons in high-temperature superconductors. *Rev. Mod. Phys.* **66**, 763 (1994).
3. Cao, Y. et al. Unconventional superconductivity in magic-angle graphene superlattices. *Nature* **556**, 43–50 (2018).
4. Jiang, H. C. & Devereaux, T. P. Superconductivity in the doped Hubbard model and its interplay with next-nearest hopping *t*′. *Science* **365**, 1424 (2019).
5. Jiang, S., Scalapino, D. J. & White, S. R. Ground-state phase diagram of the *t*-*t*′-*J* model. *Proc. Natl Acad. Sci. USA* **118**, e2109978118 (2021).
6. Li, D. et al. Superconductivity in an infinite-layer nickelate. *Nature* **572**, 624 (2019).
7. Li, D. et al. Superconducting dome in $Nd_{1-x}Sr_xNiO_2$ infinite layer films. *Phys. Rev. Lett.* **125**, 027001 (2020).
8. Zeng, S. et al. Phase diagram and superconducting dome of infinite-layer $Nd_{1-x}Sr_xNiO_2$ thin films. *Phys. Rev. Lett.* **125**, 147003 (2020).
9. Osada, M. et al. A superconducting praseodymium nickelate with infinite layer structure. *Nano Lett.* **20**, 5735–5740 (2020).
10. Osada, M., Wang, B., Lee, K., Li, D. & Hwang, H. Phase diagram of infinite layer praseodymium nickelate $Pr_{1-x}Sr_xNiO_2$ thin films. *Phys. Rev. Mater.* **4**, 121801 (2020).
11. Pan, G. A. et al. Superconductivity in a quintuple-layer square-planar nickelate. *Nat. Mater.* **21**, 160 (2022).
12. Anisimov, V. I., Bukhvalov, D. & Rice, T. M. Electronic structure of possible nickelate analogs to the cuprates. *Phys. Rev. B* **59**, 7901–7906 (1999).
13. Lee, K. W. & Pickett, W. E. Infinite-layer $LaNiO_2$: Ni^{1+} is not Cu^{2+}. *Phys. Rev. B* **70**, 165109 (2004).
14. Jiang, P., Si, L., Liao, Z. & Zhong, Z. Electronic structure of rare-earth infinite-layer $RNiO_2$ (R = La, Nd). *Phys. Rev. B* **100**, 201106 (2019).
15. Choi, M. Y., Lee, K. & Pickett, W. E. Role of 4*f* states in infinite-layer $NdNiO_2$. *Phys. Rev. B* **101**, 020503 (2020).
16. Botana, A. S. & Norman, M. R. Similarities and Differences between $LaNiO_2$ and $CaCuO_2$ and Implications for Superconductivity. *Phys. Rev. X* **10**, 011024 (2020).
17. Wu, X. et al. Robust $d_{x^2-y^2}$-wave superconductivity of infinite-layer nickelates. *Phys. Rev. B* **101**, 060504 (2020).
18. Jiang, M., Berciu, M. & Sawatzky, G. A. Critical nature of the Ni spin state in doped $NdNiO_2$. *Phys. Rev. Lett.* **124**, 207004 (2020).
19. Sakakibara, H. et al. Model construction and a possibility of cuprate-like pairing in a new d^9 nickelate superconductor (Nd,Sr)NiO_2. *Phys. Rev. Lett.* **125**, 077003 (2020).
20. Zhang, G., Yang, Y. & Zhang, F. Self-doped Mott insulator for parent compounds of nickelate superconductors. *Phys. Rev. B* **101**, 020501 (2020).
21. Karp, J. et al. Many-body electronic structure of $NdNiO_2$ and $CaCuO_2$. *Phys. Rev. X* **10**, 10.021061 (2020).
22. Hepting, M. et al. Electronic structure of the parent compound of superconducting infinite-layer nickelates. *Nat. Mater.* **19**, 381 (2020).
23. Emily, B. et al. Electronic structure trends across the rare-earth series in superconducting infinite-layer nickelates. *Phys. Rev. X* **11**, 011050 (2021).
24. Lu, H. et al. Magnetic excitations in infinite-layer nickelates. *Science* **373**, 213–216 (2021).
25. Zaanen, J., Sawatzky, G. A. & Allen, J. W. Band gaps and electronic structure of transition-metal compounds. *Phys. Rev. Lett.* **55**, 418–421 (1985).
26. Chen, Z. et al. Electronic structure of superconducting nickelates probed by resonant photoemission spectroscopy. *Matt* **5**, 1–10 (2022).
27. Chen, C. T. et al. Electronic states in $La_{2-x}Sr_xCuO_{4+\delta}$ probed by soft-x-ray absorption. *Phys. Rev. Lett.* **66**, 104–107 (1991).
28. Ruan, W. et al. Relationship between the parent charge transfer gap and maximum transition temperature in cuprates. *Sci. Bull.* **61**, 1826–1832 (2016).
29. Weber, C., Yee, C., Haule, K. & Kotliar, G. Scaling of the transition temperature of hole-doped cuprate superconductors with the charge-transfer energy. *EPL* **100**, 37001 (2012).
30. Hirsch, J. & Marsiglio, F. Hole superconductivity in infinite-layer nickelates. *Phys. C.* **566**, 1353534 (2019).
31. Kitatani, M. et al. Nickelate superconductors-a renaissance of the one-band Hubbard model. *npj Quantum Mater.* **5**, 59 (2020).
32. Leonov, I. Effect of lattice strain on the electronic structure and magnetic correlations in infinite-layer (Nd,Sr)NiO_2. *J. Alloy. Compd.* **883**, 160888 (2021).
33. Li, Y. et al. Impact of cation stoichiometry on the crystalline structure and superconductivity in nickelates. *Front. Phys.* **9**, 719534 (2021).
34. Lee, K. et al. Linear-in-temperature resistivity for optimally superconducting (Nd,Sr)NiO_2. *Nature* **619**, 288–292 (2023).
35. Wang, N. N. et al. Pressure-induced monotonic enhancement of T_c to over 30 K in superconducting $Pr_{0.82}Sr_{0.18}NiO_2$ thin films. *Nat. Commun.* **13**, 4367 (2022).
36. Rossi, M. et al. Orbital and spin character of doped carriers in infinite-layer nickelates. *Phys. Rev. B* **104**, L220505 (2021).
37. Shen, Y. et al. Role of oxygen states in the low valence nickelate $La_4Ni_3O_8$. *Phys. Rev. X* **12**, 011055 (2022).
38. Lang, Z., Jiang, R. & Ku, W. Proposal to improve Ni-based superconductors via enhanced charge transfer. *Phys. Rev. B* **105**, L100501 (2022).
39. Ivashko, O. et al. Strain-engineering Mott-insulating La_2CuO_4. *Nat. Commun.* **10**, 786 (2019).
40. Lanzara, A. et al. Evidence for ubiquitous strong electron-phonon coupling in high-temperature superconductors. *Nature* **412**, 510 (2001).
41. Tallon, J. L., Islam, R. S., Storey, J., Williams, G. V. M. & Cooper, J. R. Isotope effect in the superfluid density of high-temperature superconducting cuprates: stripes, pseudogap, and impurities. *Phys. Rev. Lett.* **94**, 237002 (2005).
42. Reznik, D. et al. Electron-phonon coupling reflecting dynamic charge inhomogeneity in copper oxide superconductors. *Nature* **440**, 1170 (2006).
43. He, Y. et al. Rapid change of superconductivity and electron-phonon coupling through critical doping in Bi-2212. *Science* **362**, 62–65 (2018).
44. Mishchenko, A. S. & Nagaosa, N. Electron-phonon coupling and a polaron in the *t*-*J* model: from the weak to the strong coupling regime. *Phys. Rev. Lett.* **93**, 036402 (2004).
45. Chen, Z. et al. Anomalously strong near-neighbor attraction in doped 1D cuprate chains. *Science* **373**, 1235–1239 (2021).
46. Giannozzi, P. et al. QUANTUM ESPRESSO: a modular and open-source software project for quantum simulations of materials. *J. Phys. Condens. Matter* **21**, 395502 (2009).
47. Perdew, J. P., Burke, K. & Ernzerhof, M. Generalized gradient approximation made simple. *Phys. Rev. Lett.* **77**, 3865–3868 (1996).
48. Blöchl, P. E. Projector augmented-wave method. *Phys. Rev. B* **50**, 17953–17979 (1994).
49. Monkhorst, H. J. & Pack, J. D. Special points for Brillouin-zone integrations. *Phys. Rev. B* **13**, 5188 (1976).
50. Mostofi, A. A. et al. wannier90: A tool for obtaining maximally-localised Wannier functions. *Comput. Phys. Commun.* **178**, 685–699 (2008).

Acknowledgements

We thank Zhuoyu Chen, Chunjing Jia, Mingda Li, Krzysztof Wohlfeld, and Fu-Chun Zhang for helpful discussions. We also acknowledge John Freeland for experimental assistance on XAS and Chendi Xie for assistance on first-principles simulations. The experimental part of this work was supported by the National Natural Science Foundation of China (Grant No. 12074411) and (Grant No. 11888101), the National Key Research and Development Program of China (Grant No. 2016YFA0300300 and 2017YFA0302900), the Strategic Priority Research Program (B) of the Chinese Academy of Sciences (Grant No. XDB25000000) and the Research Program of Beijing Academy of Quantum Information Sciences (Grant No. Y18G06). Work at MIT (J.J.S., J.L., and R.C.) was supported by the Air Force Office of Scientific Research Young Investigator Program under grant FA9550-19-1-0063. Work at Clemson and Emory University (W.C.C., J.H. and Y.W.) was supported by the National Science Foundation award DMR-2132338 and the Air Force Office of Scientific Research Young Investigator Program under grant FA9550-23-1-0153, respectively. The first-principles and model-based spectral simulations used resources of the National Energy Research Scientific Computing Center (NERSC), a U.S. Department of Energy Office of Science User Facility operated under Contract No. DE-AC02-05CH11231. The XAS measurement performed at the Advanced Photon Source was supported by the U.S. Department of Energy, Office of Science, and Office of Basic Energy Sciences under Contract No. DE-AC02-06CH11357.

Author contributions

X. J. Z. and Z. H. Z. conceived and directed the project. X. L. R. and Q. G. prepared and characterized the film samples. X. L. R., Q. G, and H. L. L. performed the transport and STEM measurements. W. C. C., J. H., and Y. W. performed the theoretical and numerical calculations. J. L., J. J. S., F. R., J. L. M, R. C. conducted the XAS measurements. X. L. R., Z. H. Z., and X. J. Z. analyzed the data. Y. W, T. X., and J. P. H., provided theoretical understanding. X. L. R., Y. W., and Z. H. Z. wrote the manuscript with input from all authors.

Competing interests

The authors declare no competing interests.

Additional information

Supplementary information The online version contains supplementary material available at https://doi.org/10.1038/s42005-023-01464-x.

Correspondence and requests for materials should be addressed to Yao Wang, Xingjiang Zhou or Zhihai Zhu.

Peer review information *Communications Physics* thanks the anonymous reviewers for their contribution to the peer review of this work. A peer review file is available.